Supporting Information

Rational Design of Metal-Organic Frameworks featuring Macrocycle and Helical Chain Motifs for Propylene/Propane Separation

Xinyu Yu,[a] Xin Huang,[a] Mengchu Feng,[a] Yuanyuan Zhang,[a,] and Bo Wang[a,]**

[a] Frontiers Science Center for High Energy Material, Key Laboratory of Cluster Science, Ministry of Education, Beijing Key Laboratory of Photoelectronic/Electrophotonic Conversion Materials, Advanced Research Institute of Multidisciplinary Science, Advanced Technology Research Institute (Jinan), School of Chemistry and Chemical Engineering, Beijing Institute of Technology, Beijing, 100081, China

Corresponding authors: bowang@bit.edu.cn, yuanyuan.zhang@bit.edu.cn

Materials

All chemicals and solvents were purchased from commercial suppliers and used without further purification. $Zn(NO_3)_2 \cdot 6H_2O$ (99.9%) was purchased from Xilong Science Co., Ltd, $Ni(NO_3)_2 \cdot 6H_2O$ (AR) was purchased from Beijing Yili Fine Chemicals Co., Ltd, and $Cu(NO_3)_2 \cdot 3H_2O$ (99.9%) was purchased from Aladdin Holdings Group Co., Ltd. 4,4'-(1H,1'H-[2,2'-biimidazole]-1,1'-diyl) dibenzoic acid (H_2BDA) was purchased from Jilin Chinese Academy of Sciences Yanshen Technology Co., Ltd. Dimethylformamide (DMF), ethanol (EtOH), and ammonia (25-28 w%) were purchased from Beijing Tong Guang Fine Chemicals Company. C_3H_6

(99.9%), C_3H_8 (99.999%), N_2 (99.9999%), and He (99.9999%) were purchased from Beijing Huatong Jingke Gas Chemical Co., Ltd.

Methods

Single-crystal X-ray diffraction data were collected at 298 K on a Bruker Smart Apex CCD area Bruker APEX-II CCD diffractometer using Mo Kα radiation tuned to λ = 0.71073 Å. The structures were solved by direct methods and refined by full-matrix least-squares on F^2 using the Bruker SHELXTL-2018 package.

Powder X-ray diffraction (PXRD) patterns of the samples were measured by a Rigaku MiniFlex 600 diffractometer operating at 40 kV voltage and 50 mA current with Cu-Kα X-ray radiation (λ = 0.154056 nm) and recorded from 1.5 to 30° (2θ) at a scan rate of 10^o min^{-1}.

Fourier transform infrared (FTIR) spectra were recorded at the range 400-4000 cm^{-1} on a Bruker ALPHA spectrometer.

Field-emission scanning electron microscopy (FE-SEM) images were obtained from a JEOL model JSM-7500F scanning electron microscope at 10 kV.

Elemental analyses (C, H, N) were conducted on an Elementar Elemental Analyser.

Thermogravimetric Analysis (TGA) was performed by a Hitachi thermogravimetric differential thermal analyzer (EXSTAR TG/DTA7000) in the temperature range of 35 °C to 800 ºC under N_2 flow at a heating rate of 10 °C min^{-1}. Prior to TGA test, freshly prepared MOF samples were washed with DMF and EtOH, and activated. BIT-

23 and BIT-24 were activated at 130 °C and 150 °C under vacuum for 8 h. BIT-25 was rinsed with acetone for 48 h through Soxhlet extractor and then activated under vacuum at 60 °C for 8 h.

CO_2 sorption isotherms were measured at 195 K and 273 K using a Quantachrome Instrument ASiQMVH002-5. The pore size distributions were calculated using the CO_2 isotherm measured at 273 K based on carbon density functional theory (NLDFT). All samples were tested with CO_2 (99.999%).

Propane and propylene sorption isotherms were measured on a BEL Japan BELSORP-max II.

Kinetic adsorption of propane and propylene were measured via a four-station BSD-DVS intelligent gravimetric analyzer, with flow set to 20 mL min^{-1}, and each sample was subjected to a constant flow rate of 5 mL min^{-1}. Before gas adsorption measurements, the BIT-MOF samples were activated. The materials were tested under the condition of 25 °C and 1 bar.

Calculation of the diffusional time constant

The diffusional time constant $D'(D_c/r_c^2)$ can be derived from the micropore diffusion model (eq. 1),[1] where m_t is the gas uptake at time t, m_∞ is the gas uptake at equilibrium, D_c is the intracrystalline diffusivity of gas molecules in porous media, and r_c is the radius of the equivalent spherical particle. D' can be obtained from the square of the slope ($\frac{m_t}{m_\infty}$ plotted against $\sqrt{t}$) multiplied by π/36.

$$\frac{m_t}{m_\infty} \approx \frac{6}{r_c}\sqrt{\frac{D_c t}{\pi}} \quad (1)$$

Calculation of isosteric heat of adsorption

The isosteric heat of adsorption profiles for C_3H_6 and C_3H_8 were derived from adsorption isotherms measured at 288 K, 298 K, and 303 K by the Clausius-Claperyron equation.[2]

A Virial-type expression was used (eq. 2), where p represents the pressure in atm, n represents the gas uptake in mmol g^{-1}, T represents the temperature in Kelvin, a_i and b_i are Virial coefficients independent of temperature, m and n are the numbers of coefficients required to adequately describe the isotherms.

$$\ln p = \ln n + \frac{1}{T}\sum_{i=0}^{m} a_i n^i + \sum_{j=0}^{n} b_j n^j \quad (2)$$

$$K_H = \exp(-b_0) \times \exp(\frac{-a_0}{T})$$

The isosteric heat of adsorption (Q_{st}) is calculated according to the following equation derived from the Clausius-Claperyron equation (eq. 3).

$$Q_{st} = -R\left[\frac{\partial lnp}{\partial\left(\frac{1}{t}\right)}\right]_n = -R\sum_i^m a_i\, n^i \quad (3)$$

Computational details

The Coulomb and Lennard-Jones 6-12 (LJ) potentials were applied to calculate the interactions between adsorbate-adsorbate and adsorbent-adsorbate. For atoms in the frameworks, the Lennard-Jones (LJ) parameters were taken from the DREIDING force field.[3] The models of C_3H_6 and C_3H_8 were taken from the TraPPE force field,[4] where

C_3 molecules were represented as a united atom.[5] The Mulliken charges and ESP charges, calculated by PDFT, were employed for the framework atoms and guest atoms, respectively. The generalized gradient approximation (GGA) with the Perdew-Burke-Ernzerhof (PBE) functional and the double numerical plus d-functions (DNP) basis set, DFT including dispersion correction (DFT-D) with Grimme method, and the Effective Core Potentials (ECP) were used for the PDFT simulation. Molecular dynamics (MD) simulations were carried out using the Forcite module in the NVT ensemble. The initial configurations for the MD simulations were produced by the GCMC simulation. The charges and force field are the same as for MD simulations. The Nosé-Hoover chain (NHC) thermostat[6] was used to maintain the adsorbent temperature at 298 K. The long-range electrostatic interactions were evaluated using the Ewald simulation method and the LJ interactions were calculated with a 12 Å cutoff radius. The time step used in the MD simulations was taken as 1.0 fs and a total period of 4 ns was performed.

Breakthrough experiment

In a typical breakthrough experiment, 1 g of activated BIT-MOF (the same activation procedures were used as for the TGA test) was packed in an adsorption column (6 mm in diameter × 20 cm in length) to form a fixed bed. The column was then purged with He gas at a flow rate of 2 mL min^{-1} at 1 bar for 1 h before the breakthrough experiment. A gas mixture containing of C_3H_6 and C_3H_8 was introduced to the column at 1 bar and 25 °C. A feed flow rate of 0.5 mL min^{-1} was set for the experiments with 50/50 mixture of gas. The flow rates of all gas mixtures were regulated by mass flow controllers, and

the effluent gas stream from the column was monitored by gas chromatography (TCD-Thermal Conductivity Detector, detection limit 300 ppm).

Adsorbent regeneration

After the adsorbent was saturated with C_3H_6 and C_3H_8, the column was purged with a He flow of 2 mL min^{-1} for 20 min at 25 °C and 1 bar. The columns were heated to 60 °C under a vacuum for 3 h and then cooled to 25 °C.

Synthesis details and activation method

BIT-23 was synthesized by mixing $Ni(NO_3)_2 \cdot 6H_2O$ (0.0174 g, 0.06 mmol), H_2BDA (0.0224 g, 0.06 mmol), DMF (5.5 mL), and $NH_3 \cdot H_2O$ (0.3 ml) in a sealed 20 mL Schott bottle, and the mixture was sonicated for 3 min and then heated in a preheated oven at 120 °C for 48 h under autogenous pressure. After the oven was cooled to room temperature, the resulting green crystals of BIT-23 were isolated by decanting off the mother liquor, washed with DMF and EtOH several times, and activated under vacuum at 120 °C for 8 h.

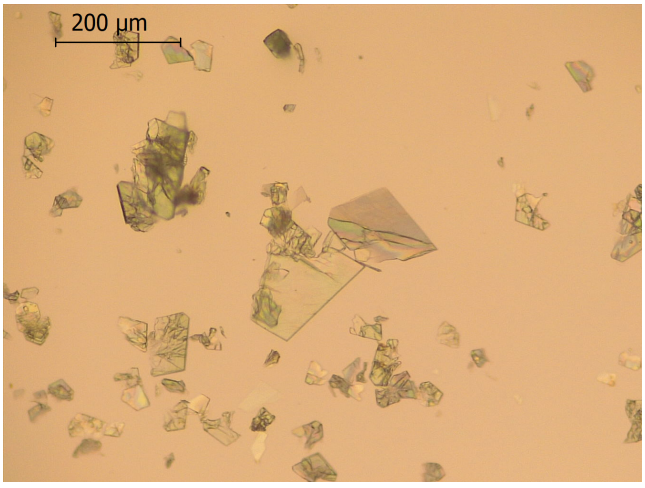

Figure S1. Optical micrograph of BIT-23.

BIT-24 and BIT-25 were synthesized using a similar procedure as BIT-23. BIT-24 was synthesized using $Zn(NO_3)_2 \cdot 6H_2O$ (0.0535 g, 0.18 mmol), H_2BDA (0.0224 g, 0.06 mmol), DMF (5.6 mL) and $NH_3 \cdot H_2O$ (0.4 ml) under the same reaction conditions as BIT-23. BIT-24 was washed with DMF and EtOH several times, and activated under vacuum at 120 °C for 8 h. BIT-25 was synthesized by $Cu(NO_3)_2 \cdot 3H_2O$ (0.0145 g, 0.06 mmol), H_2BDA (0.0224 g, 0.06 mmol), DMF (7 mL), and $NH_3 \cdot H_2O$ (0.3 ml) under the same reaction conditions. BIT-25 was washed with DMF and EtOH three times, and the rinsed with acetone for 48 h using a Soxhlet extractor, and then activated under vacuum at 60 °C for 8 h.

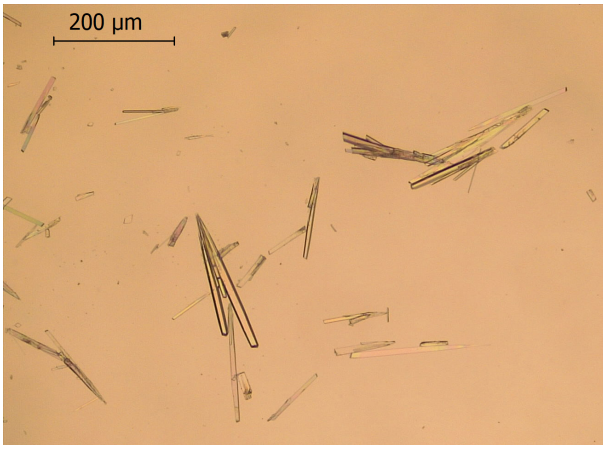

Figure S2. Optical micrograph of BIT-24.

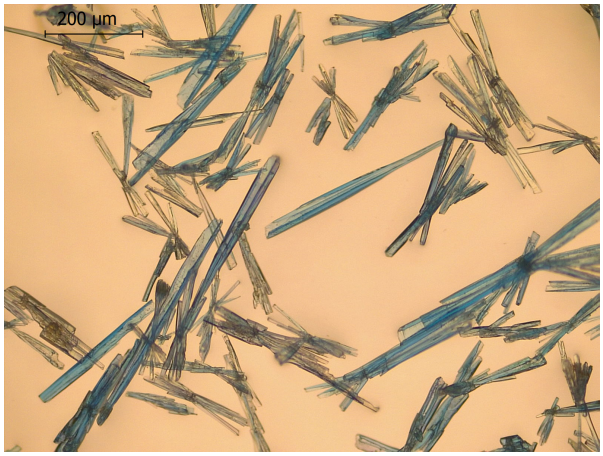

Figure S3. Optical micrograph of BIT-25.

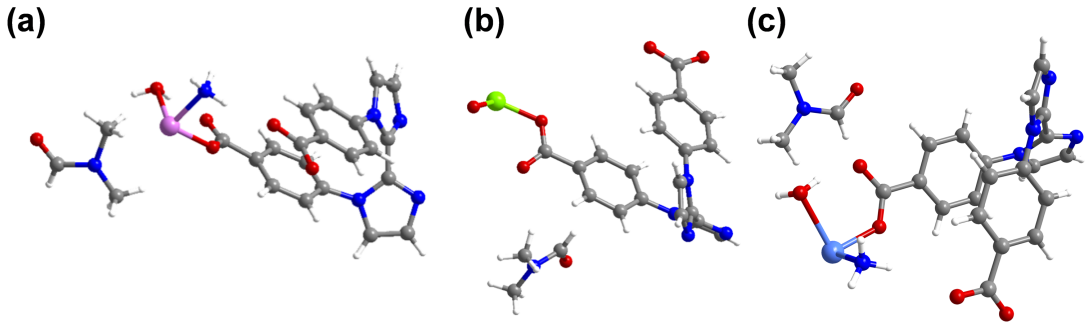

Figure S4. The asymmetric unit of (a) BIT-23, (b) BIT-24, and (c) BIT-25. Atom color scheme: O, red; C, gray; N, blue; H, white; Ni, purple; Zn, green; Cu, light blue.

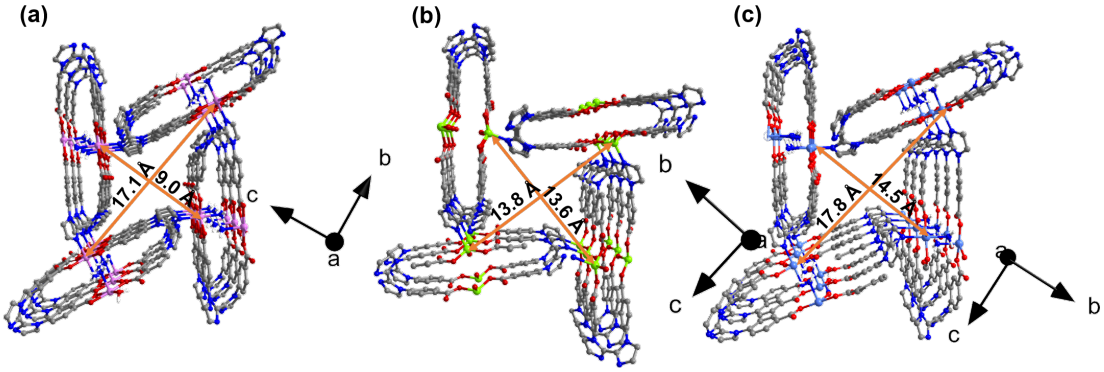

Figure S5. Crystal structure of (a) BIT-23, (b) BIT-24, and (c) BIT-25 showing 1D channels along *a*-axis. Atom color scheme: O, red; C, gray; N, blue; Ni, purple; Zn, green; Cu, light blue. Hydrogen atoms and solvent molecules are omitted for clarity.

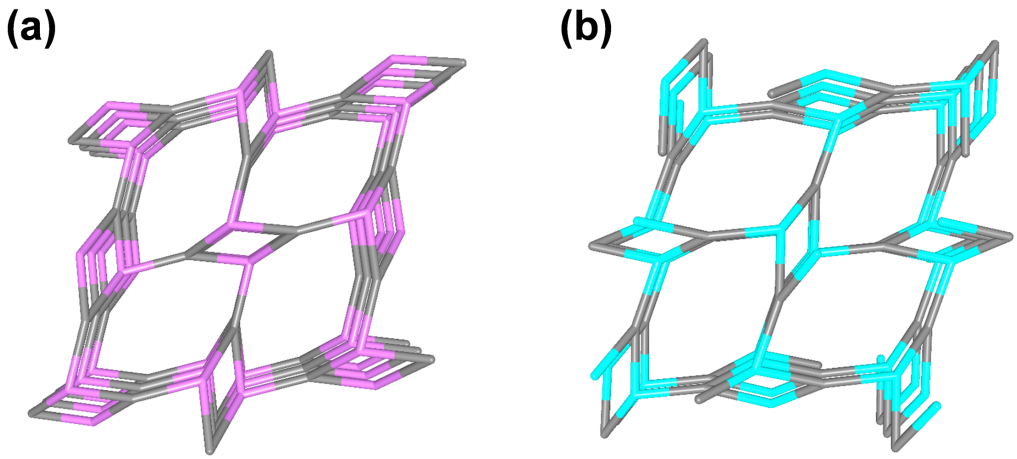

Figure S6. The topology net of (a) BIT-23 and BIT-24, and (b) BIT-25.

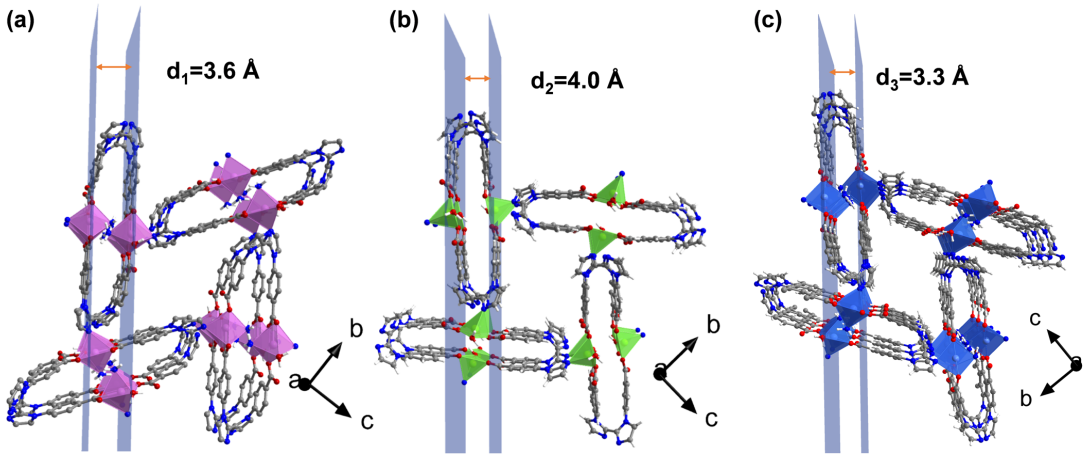

Figure S7. Distance between the two metal nodes linked by a single BDA^{2-} measured perpendicular to the direction of the 1D channel in (a) BIT-23, (b) BIT-24, and (c) BIT-25. Atom color code: O, red; C, gray; N, blue; H, white; Ni, purple; Zn, green; Cu, light blue.

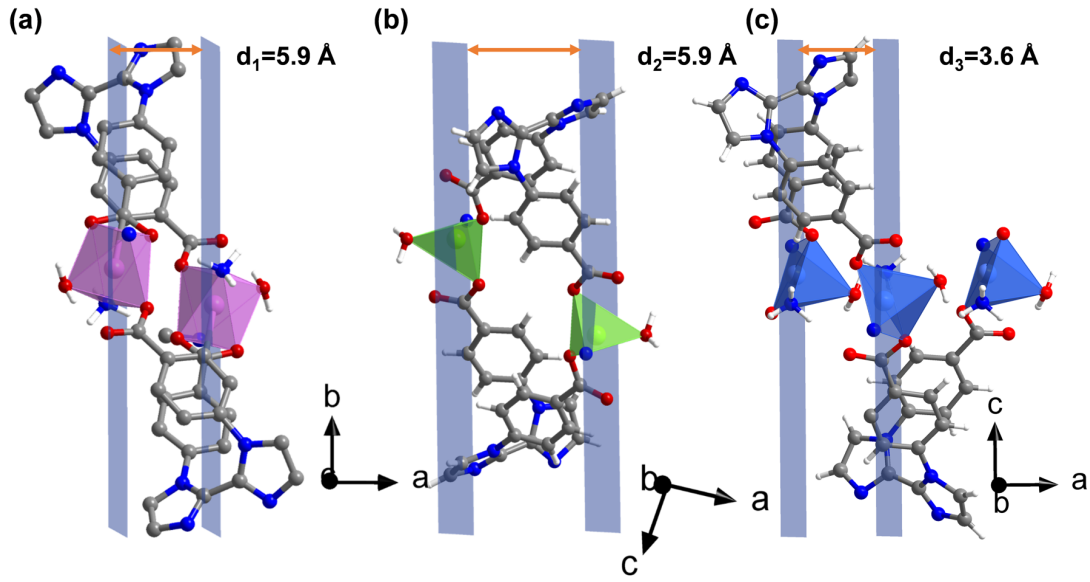

Figure S8. Distance between the two metal nodes linked by a single BDA^{2-} measured along the direction of the 1D channel in (a) BIT-23, (b) BIT-24, and (c) BIT-25. Atom color code: O, red; C, gray; N, blue; H, white; Ni, purple; Zn, green; Cu, light blue.

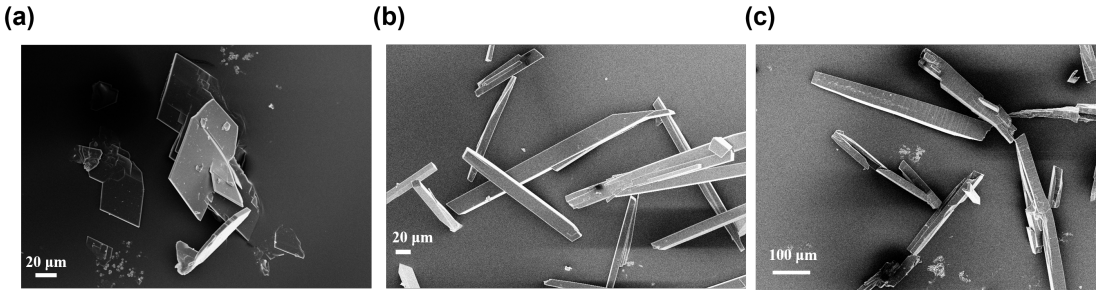

Figure S9. SEM images of the activated sample for (a) BIT-23, (b) BIT-24 and (c) BIT-25.

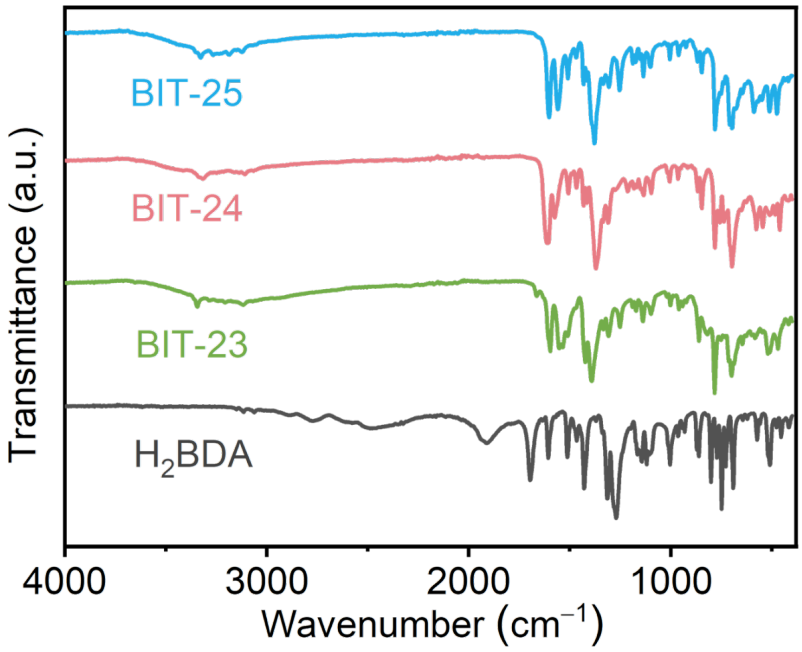

Figure S10. IR spectra of the activated sample for BIT-MOFs.

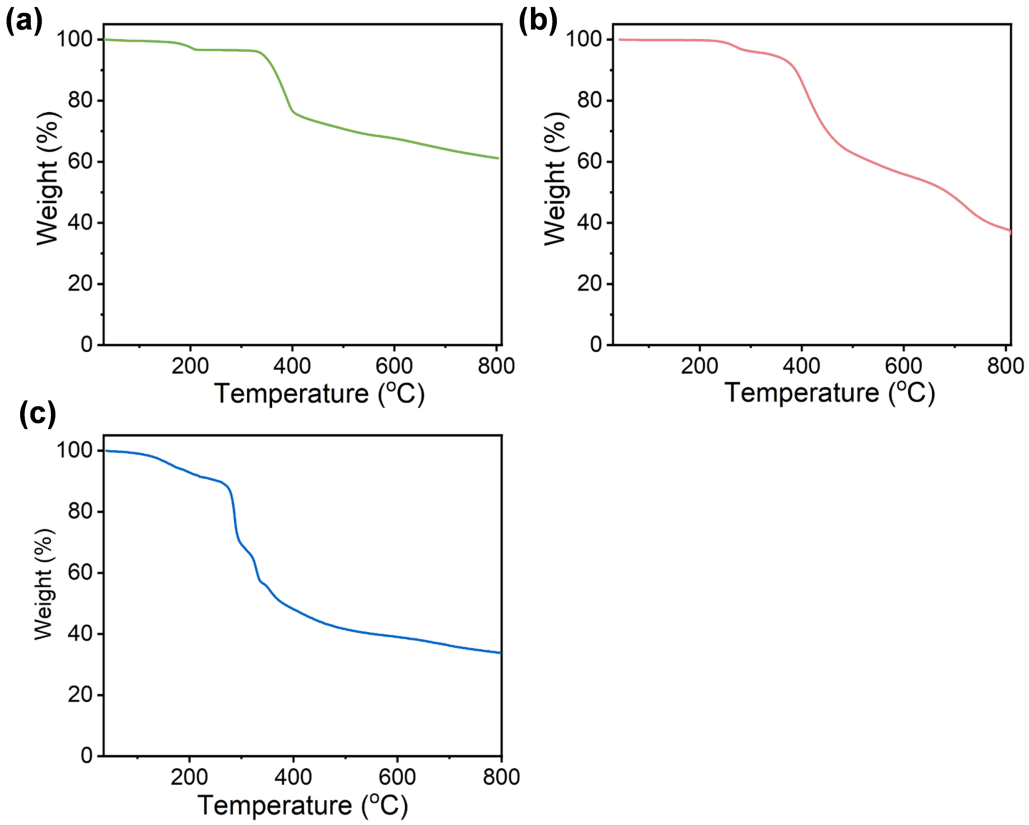

Figure S11. TGA curves of (a) BIT-23, (b) BIT-24, and (c) BIT-25 under N_2 atmosphere.

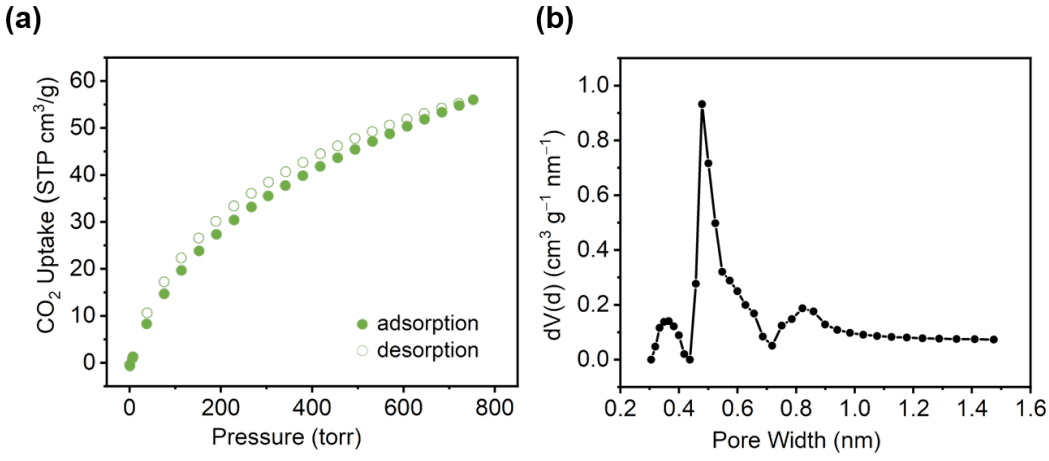

Figure S12. (a) CO_2 sorption isotherms at 273 K and (b) pore size distribution obtained using the NLDFT model for BIT-23.

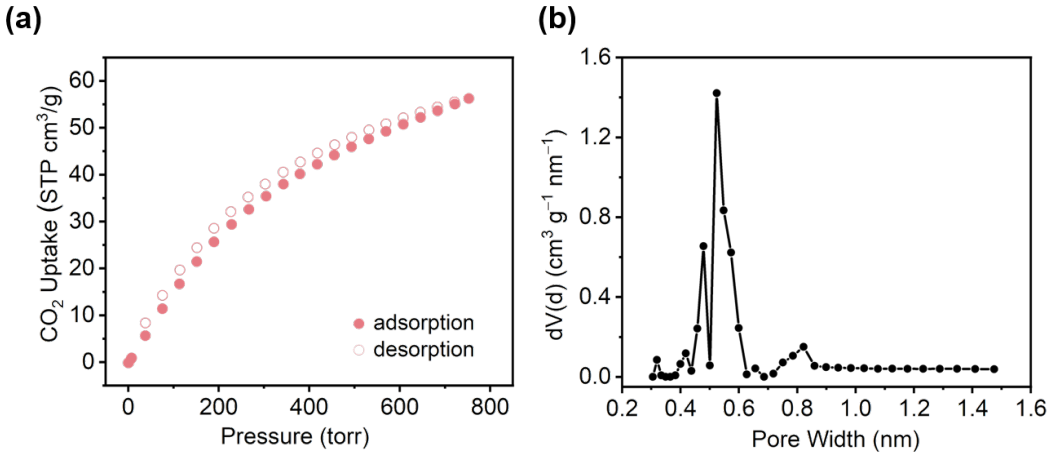

Figure S13. (a) CO_2 sorption isotherms at 273 K and (b) pore size distribution obtained using the NLDFT model for BIT-24.

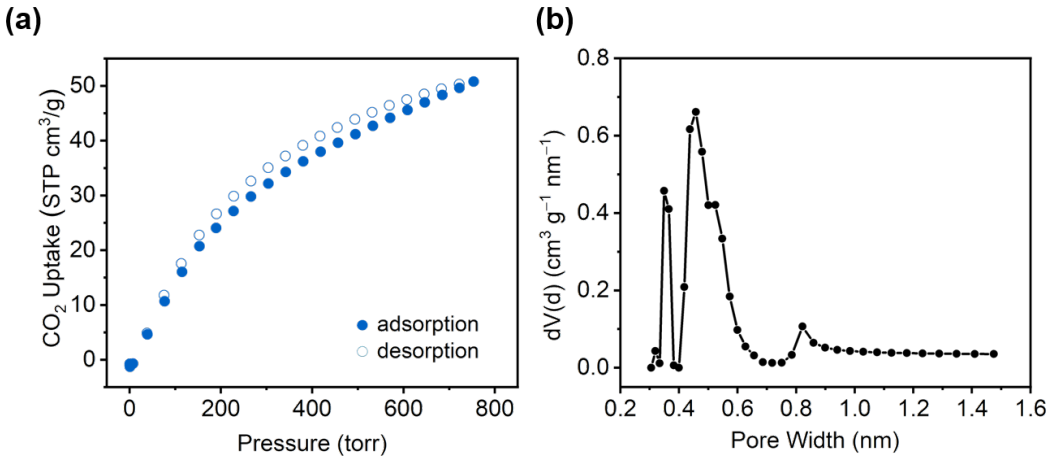

Figure S14. (a) CO_2 sorption isotherms at 273 K and (b) pore size distribution obtained using the NLDFT model for BIT-25.

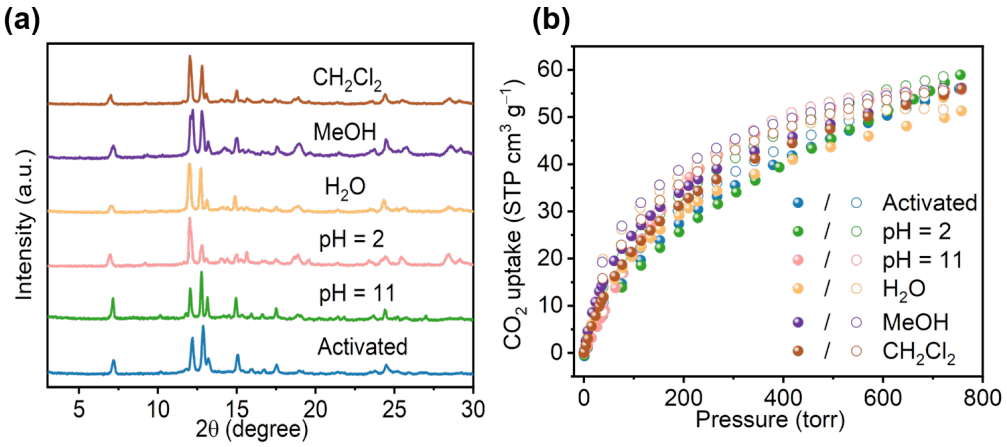

Figure S15. (a) PXRD patterns and (b) CO_2 sorption isotherms at 273 K of BIT-23 after immersing in CH_2Cl_2, MeOH, H_2O, acid aqueous solution, and alkaline aqueous solution for 12 h, respectively.

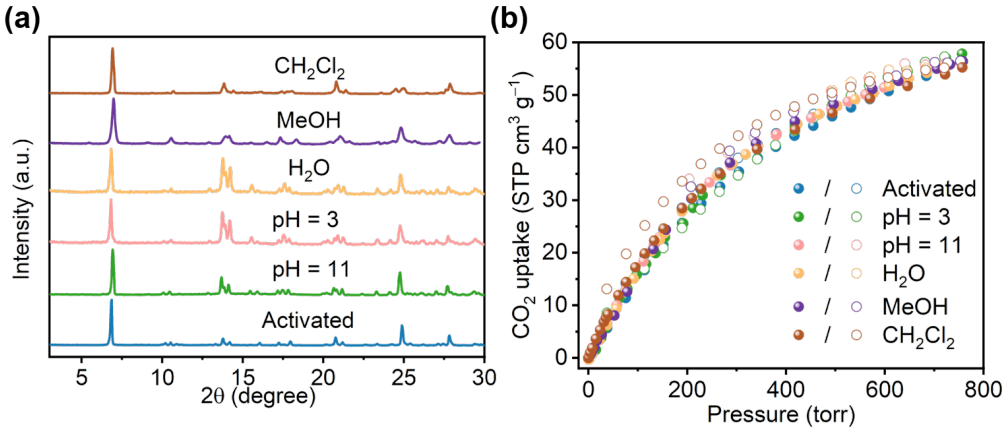

Figure S16. (a) PXRD patterns and (b) CO_2 sorption isotherms at 273 K of BIT-24 after immersing in CH_2Cl_2, MeOH, H_2O, acid aqueous solution, and alkaline aqueous solution for 12 h, respectively.

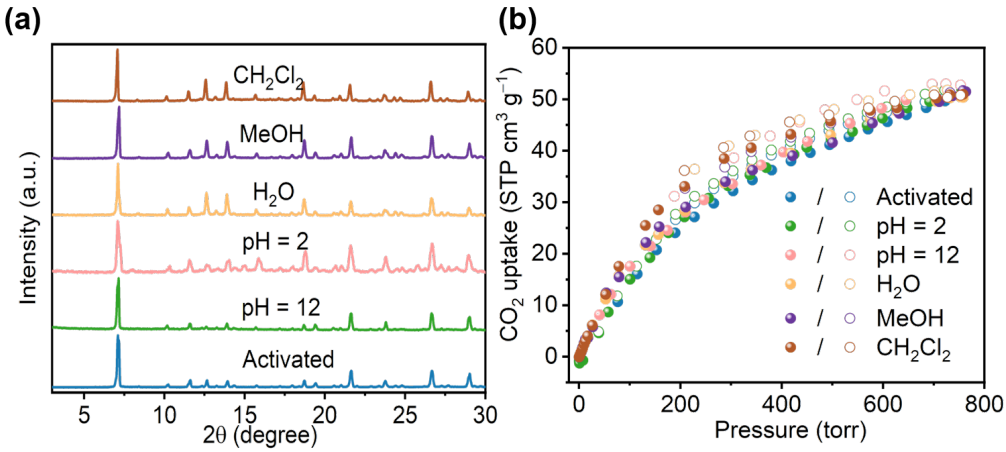

Figure S17. (a) PXRD patterns and (b) CO_2 sorption isotherms at 273 K of BIT-25 after immersing in CH_2Cl_2, MeOH, H_2O, acid aqueous solution, and alkaline aqueous solution for 12 h, respectively.

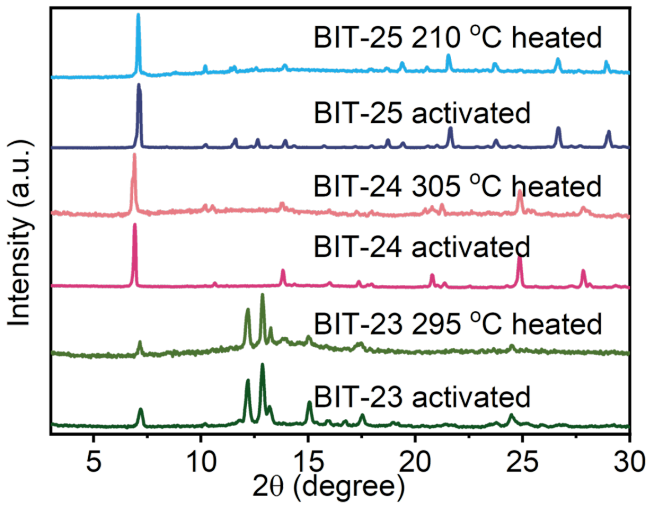

Figure S18. PXRD patterns of BIT-23, BIT-24, and BIT-25 after heating under N_2 flow.

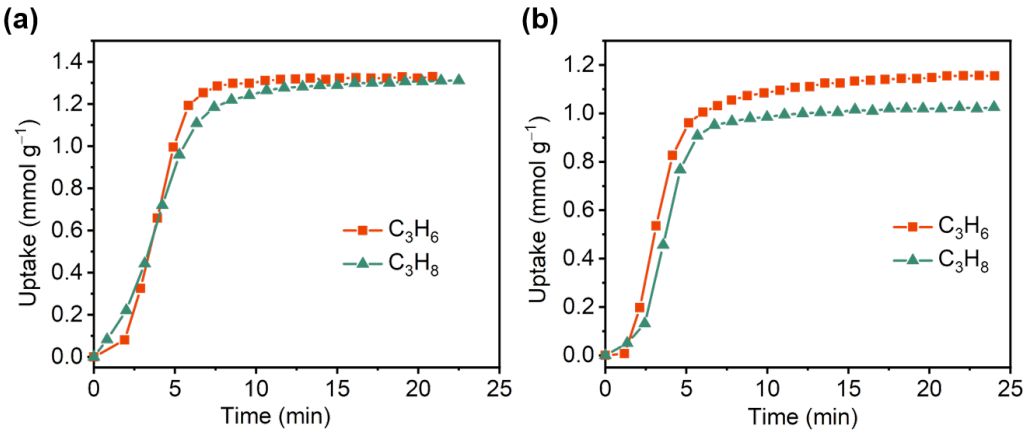

Figure S19. Kinetic adsorption profiles of C_3H_6 and C_3H_8 for (a) BIT-24 and (b) BIT-25 at 298 K and 1 bar.

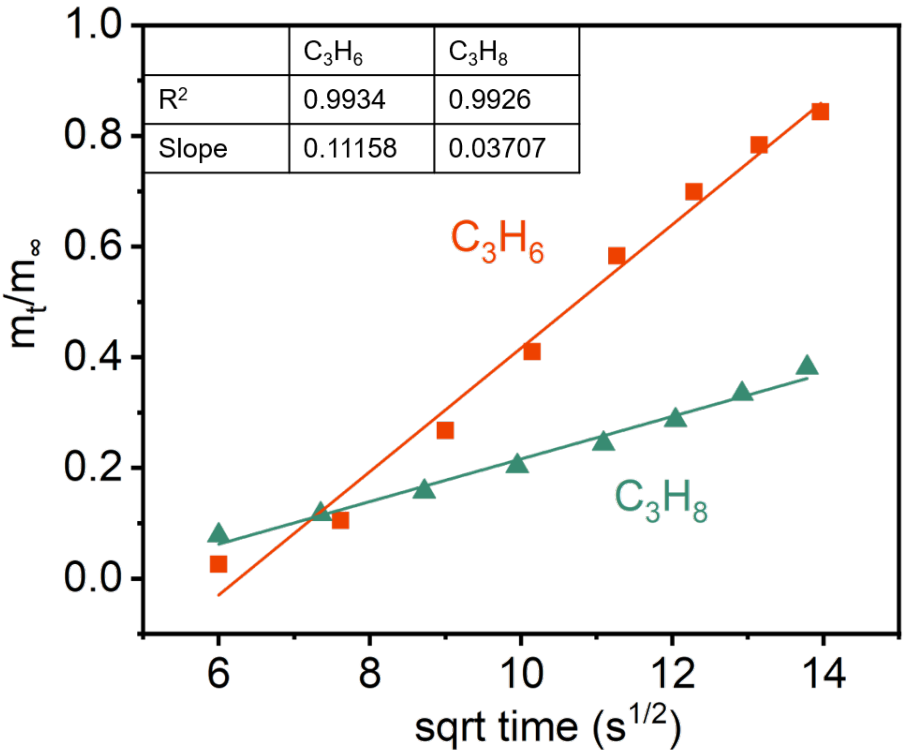

Figure S20. Fitting of diffusion time constants for C_3H_6 and C_3H_8 on BIT-23 at 298 K and 1 bar.

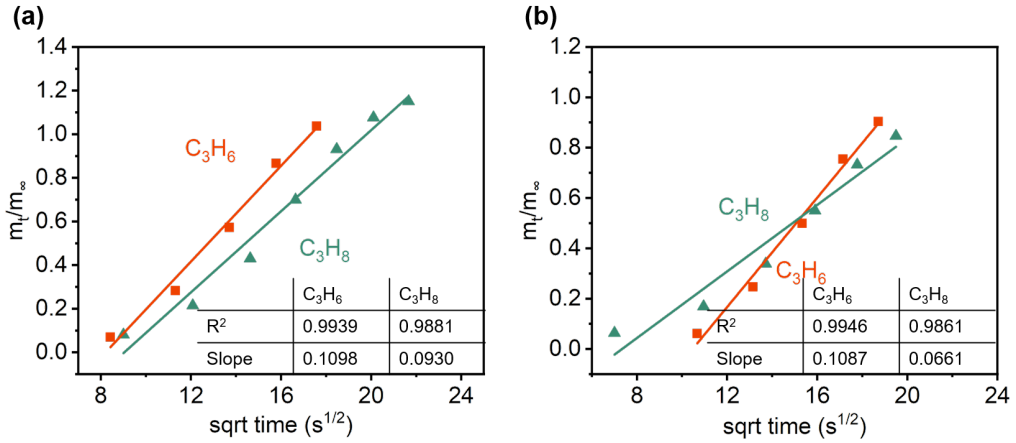

Figure S21. Fitting of diffusion time constants for C_3H_6 and C_3H_8 on (a) BIT-24 and (b) BIT-25 at 298 K and 1 bar.

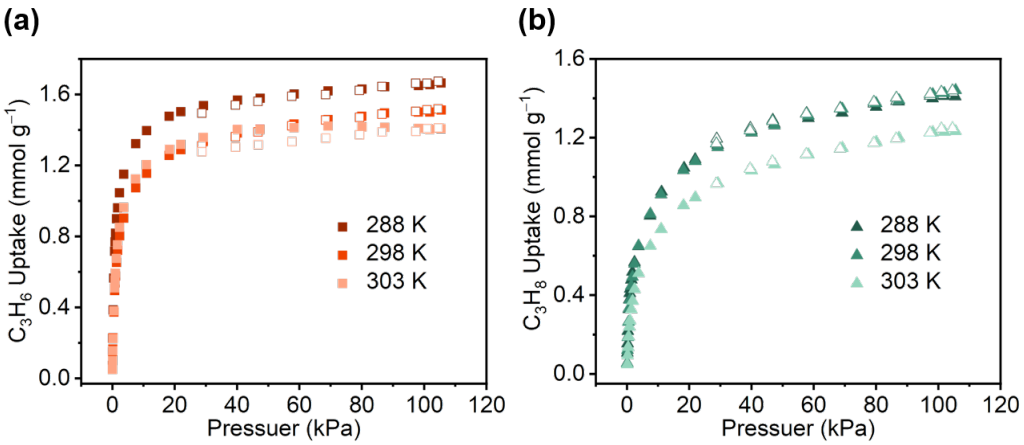

Figure S22. Single-component sorption isotherms of C_3H_6 and C_3H_8 at 288 K, 298 K, and 303 K on BIT-23.

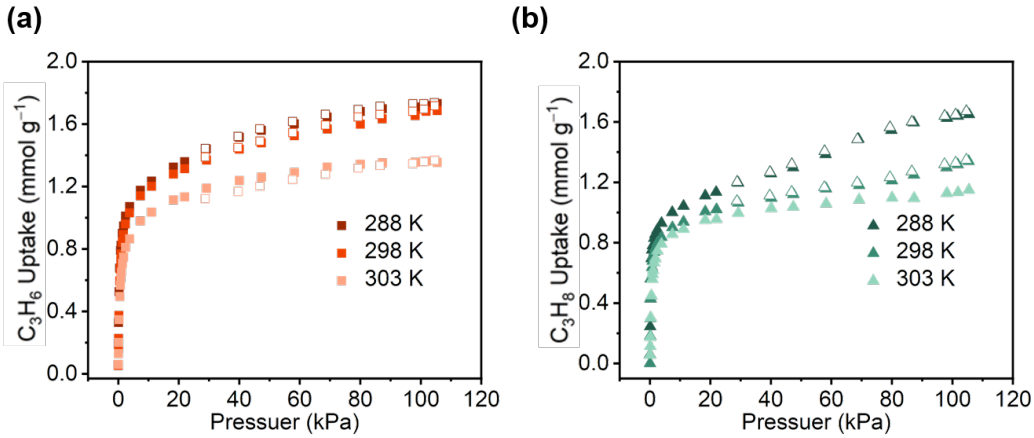

Figure S23. Single-component sorption isotherms of C_3H_6 and C_3H_8 at 288 K, 298 K, and 303 K on BIT-24.

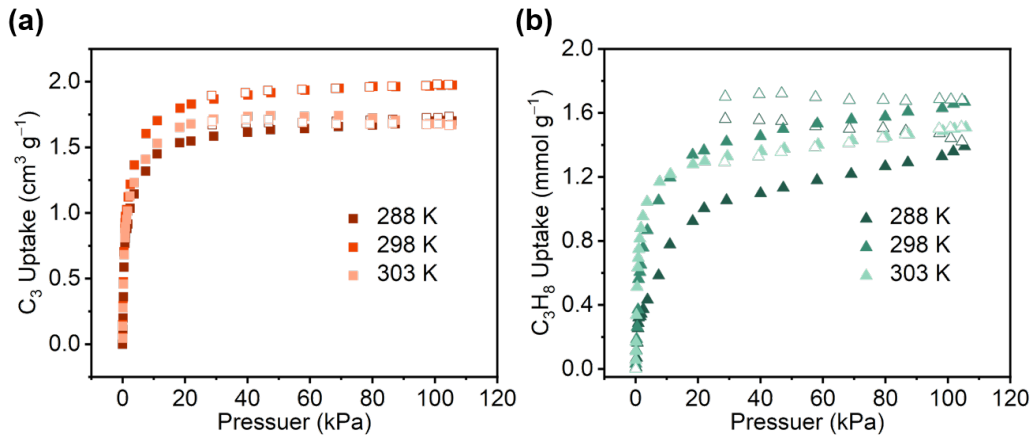

Figure S24. Single-component sorption isotherms of C_3H_6 and C_3H_8 at 288 K, 298 K, and 303 K on BIT-25.

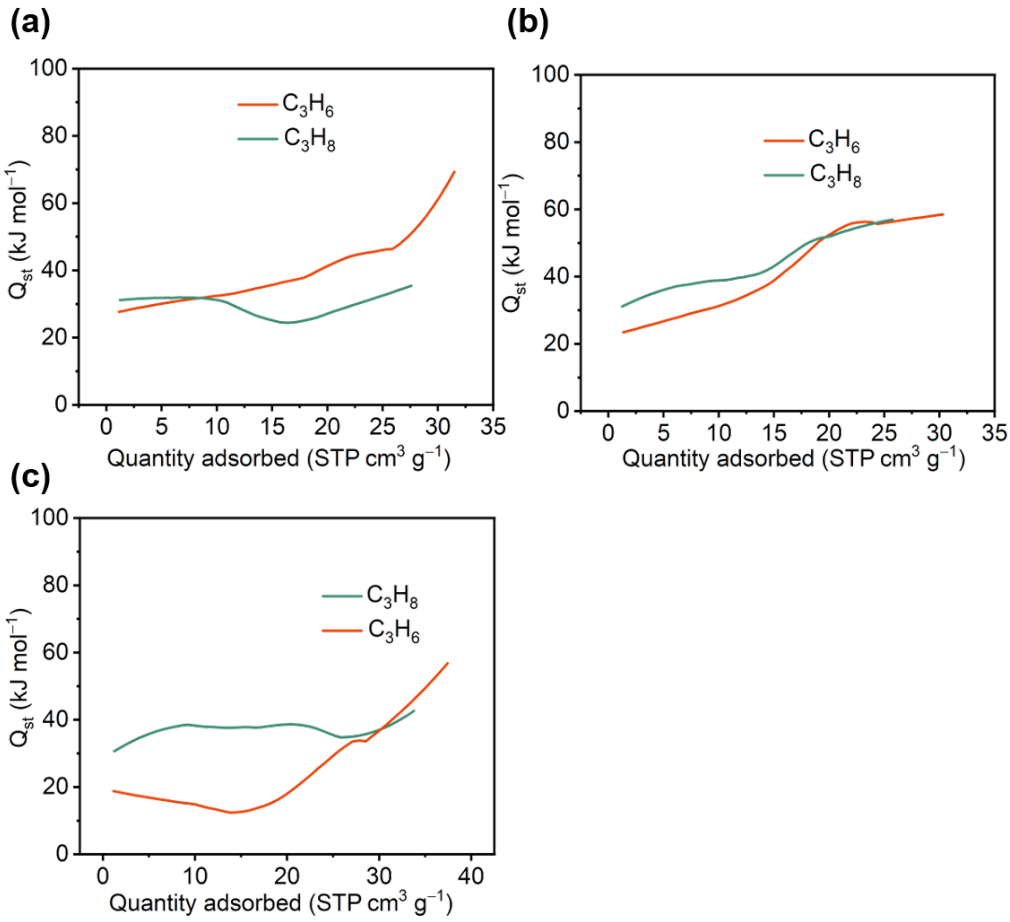

Figure S25. Isosteric heats of adsorption of C_3H_8 and C_3H_6 on (a) BIT-23, (b) BIT-24, and (c) BIT-25.

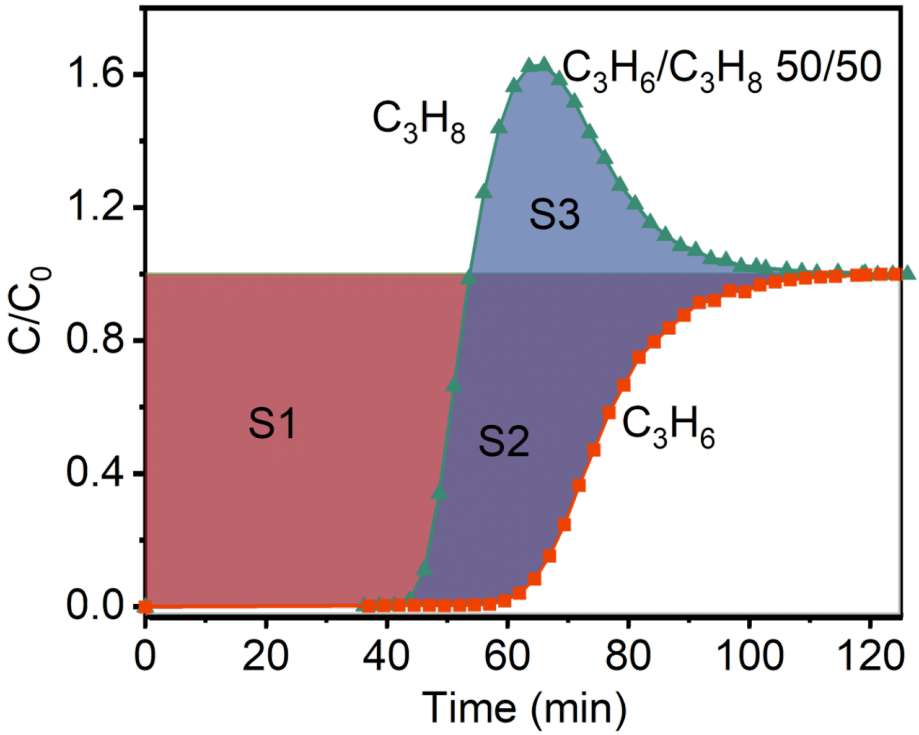

Figure S26. Calculation of the maximum adsorption capacities of C_3H_6 and C_3H_8 in breakthrough test on BIT-23.

The maximum capture amount of C_3H_6 per cycle is calculated as:

$$Q_1 = \frac{v \times V\%}{22.4 \times m} \int_{t_0}^{t_1} (c_0 - c_i)\, dt = \frac{v \times V\%}{22.4 \times m} (S1 + S2)$$

v refers to the flow rate of the gas mixture, $V\%$ refers to the molar fraction of C_3H_6, and m refers to the mass of the adsorbent.[7,8] Q_1 can thus be calculated as 0.86 mmol g^{-1}. The amount of C_3H_8 captured during t_0 to t_1 can be calculated in a similar manner as follows:

$$Q_2 = \frac{v \times V\%}{22.4 \times m} (S1 - S3) = 0.39\ mmol$$

separation factor: $\frac{Q_1}{Q_2} = 2.2$

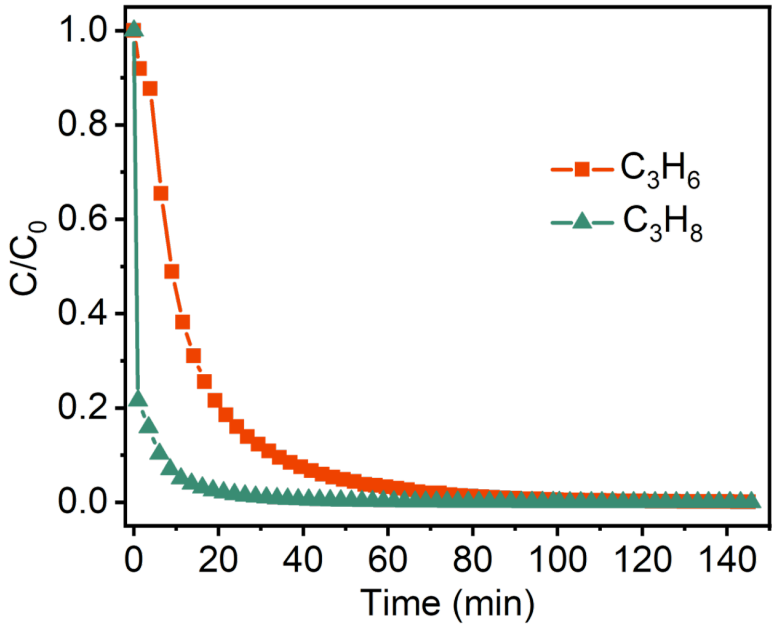

Figure S27. Experimental dynamic desorption curves of BIT-23 after breakthrough experiments with C_3H_6/ C_3H_8 (50/50). Desorption conditions: He flow rate of 1 mL/min at 100 °C. From $t_1 = 10$ min to $t_2 = 145$ min, the purity of C_3H_6 desorbed from the column is 94%.

The actual dynamic release capacity of the BIT-23 can be calculated from the integral of the desorption curve. In this paper, the dynamic release capacities of C_3H_6 and C_3H_8 are calculated from the desorption curves using the following equation[9]:

$$\mathrm{Q} = \frac{\int_{t_1}^{t_2} v C_i dt}{22.4 \times m}$$

where Q (mmol g^{-1}) is the dynamic capacity of the gas component i calculated by the desorption process, v (cm^3 min^{-1}) is the total outlet flow rate which is calculated based on the flow rate of He and the concentration of each gas component, C_i is the concentration of gas i in the outlet gas mixture, m (g) is the mass of the adsorbents, t_1 (min) is the initial calculation time, t_2 (min) is the final calculation time.

The cumulative purity p of C_3H_6 obtained by desorption process was calculated using the following equation:

$$p = \frac{Q_{C_3H_6}}{Q_{C_3H_6} + Q_{C_3H_8}} \times 100\%$$

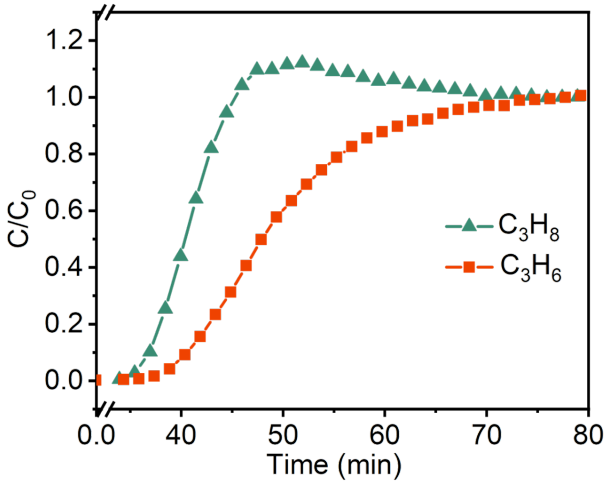

Figure S28. Dynamic breakthrough curves of BIT-24 for C_3H_8/C_3H_6 (50/50; v/v) at 298 K and 1 bar.

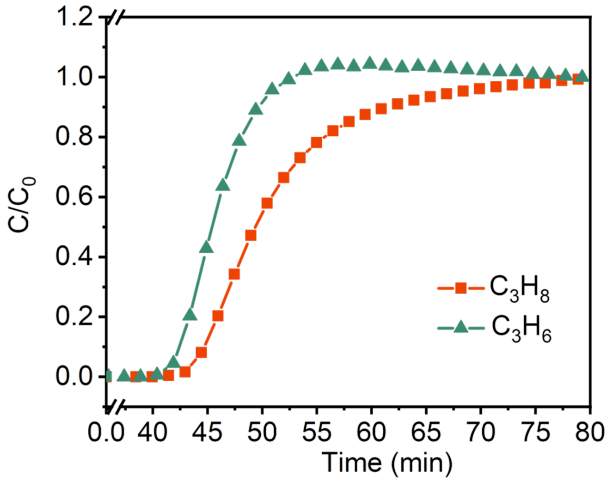

Figure S29. Dynamic breakthrough curves of BIT-25 for C_3H_8/C_3H_6 (50/50; v/v) at 298 K and 1 bar.

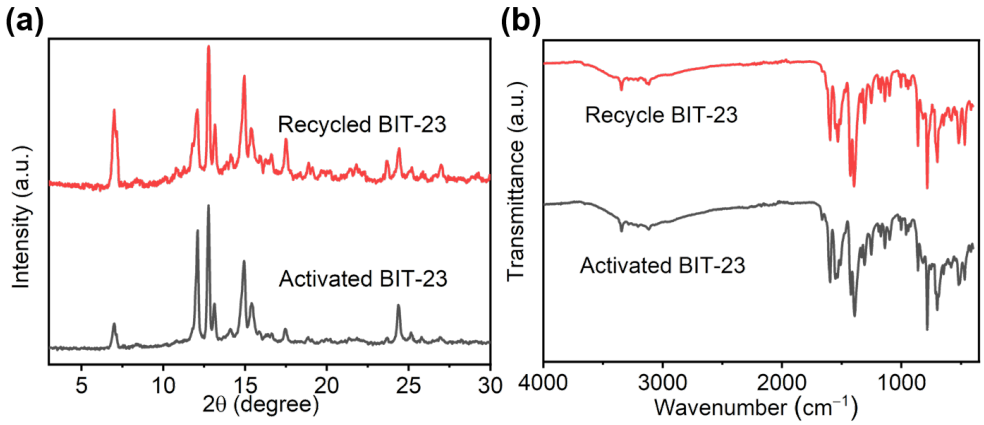

Figure S30. (a) PXRD patterns and (b) IR spectra of activated BIT-23 and recycled BIT-23.

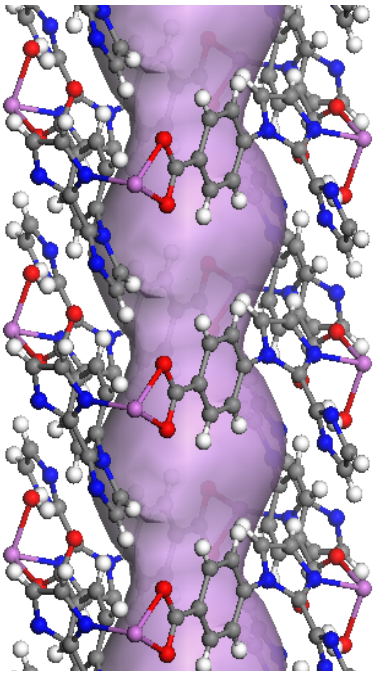

Figure S31. The Connolly surface of the BIT-23 (shown in purple). Atom color scheme: O, red; C, gray; N, blue; H, white; Ni, purple.

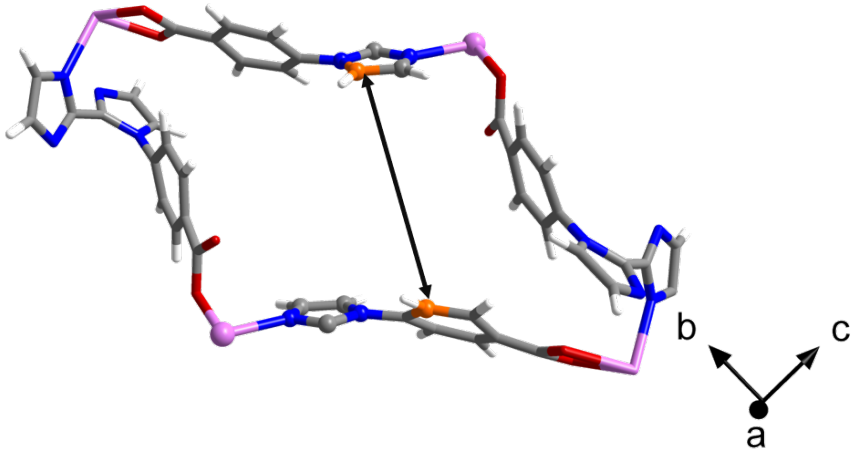

Figure S32. The narrowest distance of the bottleneck structure in BIT-23. Atom color scheme: O, red; C, gray; N, blue; H, white; Ni, purple; two carbon atoms in the shortest distance, orange.

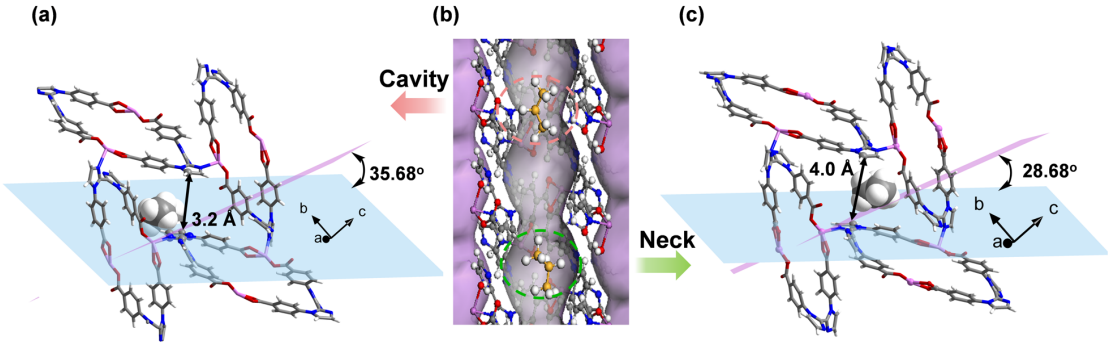

Figure S33. (a) MD simulated snapshot of the large cavity in BIT-23 with a C_3H_8 molecule (depicted in space-filling mode). (b) Connolly surface of BIT-23 with C_3H_8 molecules in the channel. The C_3H_8 is depicted in ball-stick mode with orange carbon atoms. (c) MD simulated snapshot of the bottleneck in BIT-23 with a C_3H_8 molecule (depicted in space-filling mode). The narrowest distances of the bottleneck structure in (a) and (c) are 3.2 and 4.0 Å, respectively. Color code: O, red; C, gray; N, blue; H, white; Ni, purple; the plane of the imidazole ring, grayish blue; the plane formed by linking four Ni(II) ions in two macrocycles along the *a*-axis direction, pink.

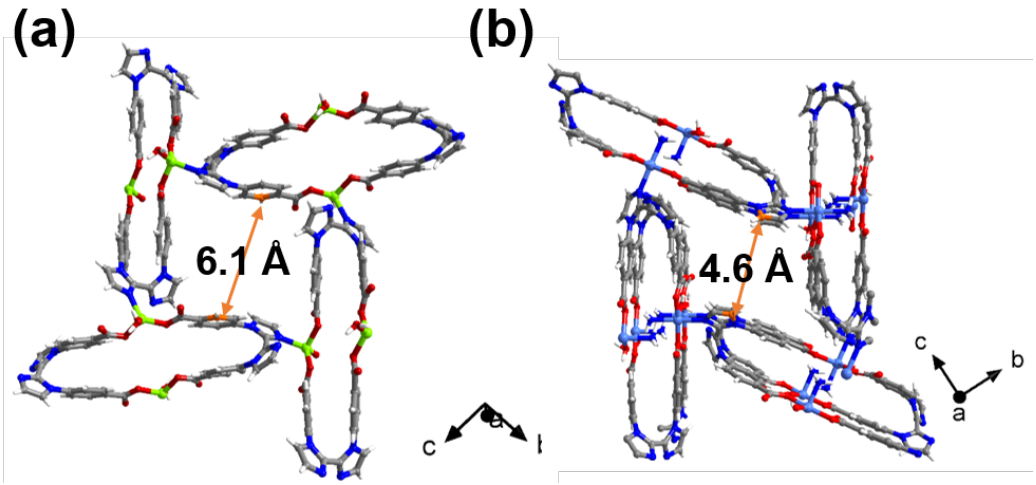

Figure S34. Crystal structures showing the narrowest distance of the channel in (a) BIT-24 and (b) BIT-25. Atom color scheme: O, red; C, gray; N, blue; H, white; Zn, green; Cu, light blue; two carbon atoms in the shortest distance, orange.

Table S1. Elemental analysis results for the activated BIT-MOFs.

	C: calcd./found	H: Calcd./found	N: Calcd./found
BIT-23	50.10/49.95	3.80/3.81	13.44/13.32
BIT-24	51.11/51.24	3.36/3.48	13.78/13.69
BIT-25	51.01/51.05	3.64/3.64	14.87/14.90

Table S2. Crystallographic data and structure refinement summary for BIT-MOFs at 298 K.

	BIT-23	BIT-24	BIT-25
Formula	[Ni(BDA)·NH_3·H_2O]·DMF	[Zn(BDA)·H_2O]·DMF	[Cu(BDA)·NH_3·H_2O]·DMF
CCDC deposition.	2174118	2174119	2174117
Formula weight (g mol^{-1})	539.2	980.6	544.0
Space group	$P2_1/c$	$P2_1/c$	$P2_12_12_1$
a(Å)	7.433	6.865	7.312
b(Å)	20.826	18.047	16.171
c(Å)	16.113	18.686	20.437
α(°)	90	90	90
β(°)	100.73	97.44	90
γ(°)	90	90	90
V ($Å^3$)	2450.6	2295.44	2416.4
Z	4	4	4
Crystal system	monoclinic	monoclinic	orthorhombic
Temperature (K)	298	298	298
ρ_{calc} (g cm^{-3})	1.461	1.419	1.495
M (mm^{-1})	0.843	1.112	0.955
F (000)	1120	1000	1124
Independent reflections	6032 [R_{int} = 0.0712, R_{sigma} = 0.0807]	5722 [R_{int} = 0.0665, R_{sigma} = 0.0478]	7311 [R_{int} = 0.0768, R_{sigma} = 0.0719]
Data/restraints/parameters	6032/74/334	5722/75/318	7311/3/334
Final R indexes [I>=2σ (I)]	R_1 = 0.0633, wR_2 = 0.1665	R_1 = 0.0561, wR_2 = 0.1561	R_1 = 0.0384, wR_2 = 0.0624
Final R indexes [all data]	R_1 = 0.1092, wR_2 = 0.1927	R_1 = 0.0900, wR_2 = 0.1783	R_1 = 0.0788, wR_2 = 0.0718
Goodness of fit on F^2	1.015	1.088	1.002

Table S3. Selected bond lengths (Å) for BIT-23.

BIT-23 bond lengths (Å)					
Ni1-O31	2.023(3)	C1-C2	1.501(5)	O4-C20	1.246(5)
Ni1-N5	2.060(3)	C2-C3	1.375(6)	N1-C11	1.372(5)
Ni1-O5	2.090(3)	C2-C7	1.391(6)	N1-C13	1.375(5)
Ni1-N32	2.110(3)	C3-C4	1.398(6)	N1-C14	1.441(5)
Ni1-O1	2.124(3)	C4-C5	1.387(6)	N2-C11	1.319(5)
Ni1-O2	2.163(3)	O6-C21	1.208(13)	N2-C12	1.373(6)
Ni1-C1	2.464(4)	C5-C6	1.384(6)	N3-C10	1.324(5)
O1-C1	1.267(5)	C6-C7	1.377(6)	N3-C9	1.377(5)
O2-C1	1.260(5)	N7-C22	1.419(13)	N4-C10	1.361(5)
O3-C20	1.252(5)	N7-C21	1.472(13)	N4-C8	1.379(5)
N7-C23	1.558(13)	C10-C11	1.458(5)	C14-C19	1.362(5)
C8-C9	1.352(6)	C12-C13	1.374(6)	C14-C15	1.385(6)
C15-C16	1.379(6)	C17-C18	1.378(6)		
C16-C17	1.394(6)	C17-C20	1.507(5)		
Symmetry code:#1 -X,-Y,-Z; #2 +X,1/2-Y,-1/2+Z					

Table S4. Selected bond angles (º) for BIT-23.

BIT-23 angles (º)					
O31-Ni1-N5	88.44(12)	C2-C1-Ni1	177.4(3)	C19-C14-C15	121.6(4)
O31-Ni1-O5	95.37(11)	C3-C2-C7	119.6(4)	C19-C14-N1	118.9(4)
N5-Ni1-O5	92.68(12)	C3-C2-C1	121.0(4)	C18-C17-C20	120.7(4)
O31-Ni1-N32	87.30(12)	C7-C2-C1	119.4(4)	C16-C17-C20	120.1(4)
N5-Ni1-N32	173.85(13)	C2-C3-C4	120.7(4)	C17-C18-C19	120.3(4)
O5-Ni1-N32	92.13(12)	C5-C4-C3	118.8(4)	C14-C19-C18	119.4(4)
O31-Ni1-O1	166.76(11)	C6-C5-C4	120.7(4)	C9-N3-Ni13	121.9(3)
N5-Ni1-O1	91.27(12)	C6-C5-N4	118.3(4)	C10-N4-C8	107.5(3)
O5-Ni1-O1	97.87(11)	C4-C5-N4	121.0(4)	C10-N4-C5	128.9(3)
N32-Ni1-O1	91.86(12)	C7-C6-C5	119.8(4)	C8-N4-C5	123.5(3)
O31-Ni1-O2	105.08(11)	C22-N7-C21	118.9(13)	O1-C1-C2	119.3(3)
N5-Ni1-O2	88.78(12)	C22-N7-C23	125.7(14)	N1-C11-C10	124.9(3)
O5-Ni1-O2	159.53(11)	C21-N7-C23	115.0(11)	N2-C12-C13	110.2(4)
N32-Ni1-O2	88.05(12)	C6-C7-C2	120.4(4)	C15-C14-N1	119.4(3)
O1-Ni1-O2	61.67(10)	C9-C8-N4	105.8(4)	C16-C15-C14	118.7(4)
O31-Ni1-C1	135.82(12)	C8-C9-N3	110.3(4)	C15-C16-C17	121.0(4)
N5-Ni1-C1	90.04(13)	N3-C10-N4	110.4(3)	C18-C17-C16	119.1(4)
O5-Ni1-C1	128.80(12)	N3-C10-C11	122.4(3)	O4-C20-O3	125.7(4)
N32-Ni1-C1	89.92(12)	N4-C10-C11	127.2(3)	O4-C20-C17	118.1(4)
O1-Ni1-C1	30.94(11)	N2-C11-N1	111.5(3)	O3-C20-C17	116.2(4)
O2-Ni1-C1	30.73(11)	C11-N1-C14	126.3(3)	O6-C21-N7	123.7(15)
C1-O1-Ni1	89.5(2)	C13-N1-C14	126.7(3)	C12-C13-N1	105.8(4)
C1-O2-Ni1	88.0(2)	C11-N2-C12	105.7(3)	C11-N1-C13	106.7(3)
C20-O3-Ni11	127.2(3)	C10-N3-C9	106.0(3)	C10-N3-Ni13	132.0(3)
N2-C11-C10	123.4(4)				
#1 -X,-Y,-Z; #2 +X,1/2-Y,-1/2+Z; #3 +X,1/2-Y,1/2+Z					

Table S5. Selected bond lengths (Å) for BIT-24.

BIT-24 bond lengths (Å)					
Zn1-O11	1.985(3)	C2-C9	1.374(5)	N3-C10	1.316(5)
Zn1-O3	2.023(3)	C2-C22	1.385(5)	N3-C19	1.384(6)
Zn1-O4	1.943(3)	C3-C17	1.352(6)	N4-C8	1.362(5)
Zn1-N12	2.042(3)	C4-C13	1.390(5)	N4-C17	1.385(5)
O1-C14	1.281(4)	C4-C14	1.498(5)	N4-C22	1.438(5)
O2-C7	1.229(5)	C4-C20	1.390(5)	N5-C1	1.430(5)
O4-C7	1.284(5)	C6-C20	1.375(5)	N5-C10	1.358(5)
O6-C14	1.231(5)	C7-C12	1.501(5)	N5-C15	1.375(5)
N1-C3	1.380(5)	C8-C10	1.469(5)	C1-C6	1.395(5)
N1-C8	1.319(5)	C9-C12	1.382(6)	C1-C18	1.380(5)
C12-C16	1.384(5)	C16-C23	1.382(5)	N2-C5	1.347(13)
C13-C18	1.385(6)	C22-C23	1.378(5)	N2-C11	1.359(11)
C15-C19	1.342(6)	O5-C5	1.280(15)	N2-C21	1.400(11)
Symmetry code:#1 1-X,1-Y,1-Z; #2 1/2-X,1/2+Y,1/2-Z					

Table S6. Selected bond angles (º) for BIT-24.

BIT-24 angles (º)					
O11-Zn1-O3	117.59(13)	O4-C7-C12	115.4(4)	C6-C20-C4	121.6(3)
O11-Zn1-N12	97.41(13)	N1-C8-N4	110.8(3)	C2-C22-N4	119.5(3)
O11-Zn1-O3	117.59(13)	N1-C8-C10	126.2(3)	C23-C22-N4	119.3(3)
O11-Zn1-N12	97.41(13)	N4-C8-C10	122.8(3)	C23-C22-C2	121.1(3)
O3-Zn1-N12	111.82(13)	C2-C9-C12	121.5(4)	C22-C23-C16	119.2(4)
O4-Zn1-O11	100.10(12)	N3-C10-N5	112.5(3)	C5-N2-C11	126.3(13)
O4-Zn1-O3	113.91(14)	N3-C10-C8	125.5(3)	C5-N2-C21	116.1(13)
O4-Zn1-N12	114.59(13)	N5-C10-C8	122.0(3)	C11-N2-C21	117.6(15)
C14-O1-Zn11	108.2(2)	C9-C12-C7	119.6(3)	O5-C5-N2	111.1(14)
C7-O4-Zn1	117.2(3)	C9-C12-C16	118.8(3)	C18-C1-C6	120.5(3)
C3-N1-Zn13	124.9(2)	C16-C12-C7	121.6(4)	C9-C2-C22	118.7(4)
C8-N1-Zn13	127.8(3)	C18-C13-C4	120.7(3)	C17-C3-N1	109.6(3)
C8-N1-C3	106.3(3)	O1-C14-C4	116.7(3)	C13-C4-C14	121.4(3)
C10-N3-C19	104.1(3)	O6-C14-O1	124.0(4)	C20-C4-C13	118.5(3)
C8-N4-C17	106.7(3)	O6-C14-C4	119.2(3)	C20-C4-C14	120.0(3)
C8-N4-C22	126.3(3)	C19-C15-N5	106.2(4)	C20-C6-C1	118.9(3)
C15-N5-C1	126.8(3)	C10-N5-C15	106.2(3)	C3-C17-N4	106.5(3)
C6-C1-N5	119.5(3)	C1-C18-C13	119.7(3)	C18-C1-N5	119.9(3)
C15-C19-N3	111.0(3)	N1-C8-N4	110.8(3)	C17-N4-C22	126.9(3)
O4-C7-C12	115.4(4)	C10-N5-C1	126.5(3)	C23-C16-C12	120.8(4)
O2-C7-O4	125.1(4)				
#1 1-X,1-Y,1-Z; :#2 1/2-X,1/2+Y,1/2-Z; :#3 1/2-X,-1/2+Y,1/2-Z					

Table S7. Selected bond lengths (Å) for BIT-25.

BIT-25 bond lengths (Å)					
Cu1-O2	1.952(2)	C1-C2	1.502(4)	O4-C20	1.234(4)
Cu1-O31	1.968(2)	C8-C9	1.358(4)	C12-C13	1.346(4)
Cu1-N5	1.990(2)	C8-N2	1.367(4)	C12-N4	1.380(4)
Cu1-N42	2.046(2)	C2-C7	1.382(4)	C4-C5	1.383(4)
Cu1-O6	2.404(2)	C2-C3	1.387(4)	O5-C23	1.227(6)
O1-C1	1.241(4)	O3-C20	1.279(4)	C5-C6	1.382(4)
N1-C10	1.363(3)	N3-C11	1.361(4)	C6-C7	1.385(4)
N1-C9	1.373(4)	N3-C13	1.377(4)	N7-C23	1.321(7)
N1-C5	1.432(4)	N3-C14	1.438(3)	N7-C22	1.425(7)
C1-O2	1.272(4)	C3-C4	1.380(4)	N7-C21	1.447(6)
N2-C10	1.316(4)	C14-C15	1.377(4)	C16-C17	1.381(4)
C10-C11	1.458(4)	C14-C19	1.379(4)	C17-C18	1.390(4)
C11-N4	1.325(4)	C15-C16	1.391(4)	C17-C20	1.507(4)
C18-C19	1.375(4)				
Symmetry code:#1 1/2+X,1/2-Y,1-Z;#2 1/2-X,1-Y,1/2+Z					

Table S8. Selected bond angles (º) for BIT-25.

BIT-25 angles (º)					
O2-Cu1-O31	170.92(10)	C5-C6-C7	119.0(3)	C15-C14-C19	121.2(3)
O2-Cu1-N5	87.62(10)	C23-N7-C22	119.5(5)	C15-C14-N3	120.5(3)
O31-Cu1-N5	90.04(9)	C23-N7-C21	120.5(5)	C19-C14-N3	118.3(3)
O2-Cu1-N42	87.55(9)	C22-N7-C21	119.9(5)	C14-C15-C16	118.7(3)
O31-Cu1-N42	93.60(9)	C2-C7-C6	120.6(3)	C18-C19-C14	119.7(3)
N5-Cu1-N42	171.25(11)	C8-C9-N1	106.0(3)	O4-C20-O3	124.1(3)
O2-Cu1-O6	97.18(8)	C10-N2-C8	105.2(2)	O4-C20-C17	119.8(3)
O31-Cu1-O6	91.72(8)	N2-C10-N1	111.8(2)	O3-C20-C17	116.1(3)
N5-Cu1-O6	93.58(10)	N2-C10-C11	123.8(2)	O5-C23-N7	126.0(6)
N42-Cu1-O6	94.26(9)	N1-C10-C11	124.3(2)	C4-C3-C2	120.8(3)
C10-N1-C9	106.4(2)	N4-C11-N3	110.4(3)	C13-C12-N4	109.7(3)
C10-N1-C5	127.0(2)	N4-C11-C10	123.8(3)	C3-C4-C5	118.9(3)
C9-N1-C5	126.1(2)	N3-C11-C10	125.7(3)	C6-C5-C4	121.2(3)
O1-C1-O2	125.6(3)	C11-N4-C12	106.1(2)	C4-C5-N1	119.9(3)
O1-C1-C2	118.9(3)	C11-N4-Cu14	131.4(2)	C11-N3-C14	128.2(2)
O2-C1-C2	115.5(3)	C12-N4-Cu14	122.51(19)	C13-N3-C14	124.7(3)
C1-O2-Cu1	126.2(2)	C12-C13-N3	106.6(3)	C6-C5-N1	118.8(3)
C9-C8-N2	110.7(3)	C20-O3-Cu13	110.81(19)	C18-C17-C20	120.4(3)
C7-C2-C3	119.3(3)	C11-N3-C13	107.1(2)	C19-C18-C17	120.3(3)
C7-C2-C1	121.0(3)	C16-C17-C18	119.2(3)	C17-C16-C15	120.8(3)
C3-C2-C1	119.5(3)	C16-C17-C20	120.4(3)		
#1 1/2+X,1/2-Y,1-Z; #2 1/2-X,1-Y,1/2+Z; #3 -1/2+X,1/2-Y,1-Z; #4 1/2-X,1-Y,-1/2+Z					

REFERENCES

1. Q. Ding, Z. Zhang, C. Yu, P. Zhang, J. Wang, L. Kong, X. Cui, C.H. He, S. Deng and H. Xing, *Aiche J.*, 2021, **67**, e17094.

2. M. Dincă, A. Dailly, Y. Liu, C.M. Brown, D.A. Neumann and J.R. Long, *J. Am. Chem. Soc.*, 2006, **128**, 16876-16883.

3. S.L. Mayo, B.D. Olafson and W.A. Goddard, *J. Phys. Chem. C*, 1990, **94**, 8897-8909.

4. A.K. Rappe, C.J. Casewit, K.S. Colwell, W.A. Goddard, III and W.M. Skiff, *J. Am. Chem. Soc.*, 1992, **114**, 10024-10035.

5. M.G. Martin and J.I. Siepmann, *J. Phys. Chem. B*, 1998, **102**, 2569-2577.

6. G.J. Martyna, M.E. Tuckerman, D.J. Tobias and M.L. Klein, *Mol. Phys.*, 1996, **87**, 1117-1157.

7. L. Wang, N. Xu, Y. Hu, W. Sun, R. Krishna, J. Li, Y. Jiang, S. Duttwyler and Y. Zhang, *Nano Res.*, 2023, **16**, 3536-3541.

8. L. Li, R.-B. Lin, X. Wang, W. Zhou, L. Jia and B. Chen, *Chem. Eng. J.*, 2018, **354**, 977-982.

9. X. Zhu, T. Ke, J. Zhou, Y. Song, Q. Xu, Z. Zhang, Z. Bao, Y. Yang, Q. Ren and Q. Yang, *J. Am. Chem. Soc.*, 2023, **145**, 9254-9263.